

Shadow and quasinormal modes of the rotating Einstein-Euler-Heisenberg black holes

Gaetano Lambiase ^{1,2,*} Dhruba Jyoti Gogoi ^{3,4,†} Reggie C. Pantig ^{5,‡} and Ali Övgün ^{6,§}

¹*Dipartimento di Fisica "E.R Caianiello", Università degli Studi di Salerno,
Via Giovanni Paolo II, 132 - 84084 Fisciano (SA), Italy.*

²*Istituto Nazionale di Fisica Nucleare - Gruppo Collegato di Salerno - Sezione di Napoli,
Via Giovanni Paolo II, 132 - 84084 Fisciano (SA), Italy.*

³*Department of Physics, Moran College, Moranhat, Charaideo 785670, Assam, India.*

⁴*Theoretical Physics Division, Centre for Atmospheric Studies,
Dibrugarh University, Dibrugarh 786004, Assam, India.*

⁵*Physics Department, Mapúa University, 658 Muralla St., Intramuros, Manila 1002, Philippines*

⁶*Physics Department, Eastern Mediterranean University,
Famagusta, 99628 North Cyprus via Mersin 10, Türkiye.*

(Dated: June 27, 2024)

The Einstein-Euler-Heisenberg (EEH) black hole model is an extension of classical black hole solutions in general relativity, incorporating quantum electrodynamics (QED) effects via the Euler-Heisenberg Lagrangian. The Euler-Heisenberg Lagrangian describes the nonlinear corrections to Maxwell's equations due to virtual electron-positron pair production in a strong electromagnetic field. When this Lagrangian is coupled with Einstein's field equations, it leads to modified black hole solutions that took into account these quantum corrections. In this paper, we investigate the impact of the screening parameter, acting as an effective dielectric constant endowed in a vacuum due to such QED effects, on the properties of the rotating and electrically charged Einstein-Euler-Heisenberg black holes (EEH). To this aim, we analyzed and discussed findings as to how the screening parameter, being positive or negative, affects certain black hole properties such as null regions, shadow cast and its observables, and quasinormal modes (QNMs) relative to the Kerr and Kerr-Newman cases. We find that the presence of a screened charge due to the associated QED effects in this screened Maxwell theory might noticeably alter the properties of black holes, offering insights into the interplay between gravity and quantum field effects.

PACS numbers: 95.30.Sf, 04.70.-s, 97.60.Lf, 04.50.+h

Keywords: Black hole; Quasinormal modes; Greybody

I. INTRODUCTION

The Event Horizon Telescope (EHT) Collaboration's work on capturing the first images of supermassive black holes is a monumental achievement in astrophysics. The EHT is a global radio telescope network that works together to form a virtual Earth-sized telescope using the Very Long Baseline Interferometry (VLBI) technique. By synchronizing multiple telescopes across different continents, the EHT can achieve the high resolution necessary to observe details as small as the event horizon of a black hole. The image of M87*, released in April 2019, was the first direct visual evidence of a black hole's existence [1–3]. It confirmed theoretical predictions based on General Relativity and provided new insights into the behavior of matter and light around supermassive black holes, first analyzed through the seminal works of Synge and Luminet [4, 5] for static black holes, and Bardeen [6] for the axisymmetric case. Then, the image of Sgr. A*, released in May 2022, provided the first visual confirmation of the black hole at the center of our galaxy. It also validated the methods developed for M87* and underscored the dynamic nature of Sgr A* [7, 8]. EHT's success has profound implications for astrophysics as it opens up new avenues for studying black holes' environments, testing gravity theories under extreme conditions, and understanding the fundamental physics of accretion and jet formation. The precise shape of these shadows encodes critical physical parameters, such as the black holes mass and spin, and the study of black hole shadows has proven instrumental in addressing fundamental questions across a broad spectrum of topics [9], including the behavior of accretion disks [10], the nature of dark matter [11, 12], modified gravity theories [13–19], and the existence of extra dimensions [20]. These intriguing questions have ignited a surge of theoretical and experimental research into black hole shadows.

The Einstein-Euler-Heisenberg system is considered an effective action of a superstring theory, where static and spherically symmetric black hole solutions were constructed in Ref. [21], and the electric charge was included [22]. The charged static case was then extended in Ref. [23] to an axisymmetric case using the Newman-Janis algorithm. Then, its rotating structure

* lambiase@sa.infn.it

† moloydhruba@yahoo.in

‡ rcpantig@mapua.edu.ph

§ ali.ovgun@emu.edu.tr

was studied [24]. Time-like particle motion was considered in Ref. [25], and many studies about the non-rotating case of EEH black holes exist in the literature [26–34]. One of the aims of this paper is to explore the properties of the rotating EEH black hole through the shadow cast, shadow radius, and observables.

Black holes, intriguing celestial entities governed by Einstein’s theory of gravity, represent enigmatic phenomena in the universe. A seminal moment in the study of black holes occurred with the detection of Gravitational Waves (GWs) on September 14th, 2015 [35]. This milestone not only deepened our understanding of black holes but also paved the way for experimental tests of gravitational theories. According to Einstein’s theory of general relativity, GWs originate from the acceleration of massive objects, causing disturbances in the fabric of spacetime. These waves carry essential information about the dynamics and kinematics of the astronomical sources that produce them. Advanced instruments such as LIGO and Virgo have played pivotal roles in detecting GWs.

When two black holes merge, they coalesce into a final black hole that emits GWs exhibiting distinct wave patterns known as ring-down modes. These GWs manifest quasinormal modes (QNMs) that depend on the mass and spin of the resulting black hole. Analyzing GW data using these QNMs is crucial for unveiling the mysterious properties of black holes and acquiring valuable insights into their nature.

QNMs represent a significant and captivating aspect of black hole physics. They signify the oscillations of a black hole that gradually attenuate over time, characterized by intricate frequencies. Termed “quasinormal” because they are not precisely normal modes, which would perpetually oscillate [36–38], they fade away due to dissipative mechanisms such as gravitational wave emission. QNMs are complex values that portray the emission of gravitational waves from compact, massive celestial objects in the cosmos. The real component of QNMs indicates the emission frequency, while the imaginary component corresponds to their decay rate. Understanding QNMs is imperative as they encode vital information about the attributes of black holes, including their mass, angular momentum, and the characteristics of the surrounding spacetime. Moreover, delving into QNMs offers insights into the nature of black holes and the strong gravitational regime, which is challenging to explore using alternative methodologies. These modes play a fundamental role in comprehending the structure and evolution of black holes and their involvement in astrophysical phenomena such as gravitational wave signals. Recent years have witnessed extensive research into the exploration of GWs and the QNMs displayed by black holes within various modified gravity theories [39–56].

The program of the paper is as follows: In Sect. II, we give a brief review of the EEH theory and the EEH rotating black hole. In Sect. III, we explore the null regions such as the event horizon and ergosphere. Sect. IV examines the null geodesic, and in Sect. V, we study the different observables such as the shadow cast, shadow radius, etc. Sect. VI examines the QNMs, both the rotating and static cases. Finally, we form a conclusion and state possible future research directions. The paper use the metric signature $(-, +, +, +)$ and geometrized units by applying $G = c = 1$.

II. BRIEF REVIEW OF EINSTEIN-EULER-HEISENBERG THEORY AND EEH ROTATING BLACK HOLE

First, we provide a brief overview of the EEH theory, which is minimally coupled to nonlinear electrodynamics (NLED) [24]

$$S = \frac{1}{4\pi G} \int_{M^4} d^4x \sqrt{-g} \left[\frac{1}{4}R - \mathcal{L}(X, Y) \right], \quad (1)$$

In this context, G represents Newton’s constant, which we set to $G = 1$. g is the determinant of the metric tensor, R is the Ricci scalar, and $\mathcal{L}(X, Y)$ is the Lagrangian of the nonlinear electrodynamics (NLED) theory. This Lagrangian is determined by the only two independent relativistic invariants derived from the Faraday tensor for the Maxwell field in four dimensions: the scalar X and the pseudoscalar Y where $X = \frac{1}{4}F_{\mu\nu}F^{\mu\nu} = \frac{1}{2}(\mathbf{B}^2 - \mathbf{E}^2)$ and $Y = \frac{1}{4}F_{\mu\nu}{}^*F^{\mu\nu} = \mathbf{E} \cdot \mathbf{B}$. In this context, \mathbf{E} and \mathbf{B} represent the electric field and the magnetic field strength, respectively. $F_{\mu\nu}$ is the Faraday electromagnetic tensor, and ${}^*F_{\mu\nu}$ is its dual, defined by ${}^*F_{\mu\nu} = \frac{1}{2}\sqrt{-g}\epsilon_{\mu\nu\sigma\rho}F^{\sigma\rho}$, $\epsilon_{0123} = -1$, and ${}^*F^{\mu\nu} = \frac{1}{2}\frac{1}{\sqrt{-g}}\epsilon^{\mu\nu\sigma\rho}F_{\sigma\rho}$, $\epsilon^{0123} = 1$, $\epsilon_{\mu\nu\sigma\rho}$ is completely antisymmetric and satisfies $\epsilon_{\mu\nu\sigma\rho}\epsilon^{\mu\nu\sigma\rho} = -4!$.

Note that for the EEH theory [57],

$$\mathcal{L}(X, Y) = -X + \frac{2\alpha^2}{45m^4} (4X^2 + 7Y^2). \quad (2)$$

In the case of the Euler-Heisenberg theory, where m is the electron mass and α is the fine structure constant, the theory reverts to linear Maxwell electrodynamics when $\alpha = 0$ and $\mathcal{L}(X) = -X$. The Einstein equations are derived by varying the action given with respect to the metric $g_{\mu\nu}$. $G_{\mu\nu} = 8\pi T_{\mu\nu}$ where $G_{\mu\nu}$ represents the Einstein field tensor, and the energy-momentum tensor $T_{\mu\nu}$ is given by the derivative of \mathcal{L} with respect to the corresponding invariant. The variation with respect to the electromagnetic four-potential A_μ yields the electromagnetic field equations

$$\nabla_\mu (\mathcal{L}_X F^{\mu\nu} + \mathcal{L}_Y {}^*F^{\mu\nu}) = 0, \quad (3)$$

and the energy-momentum tensor is

$$T_{\mu\nu} = \frac{1}{4\pi} [g_{\mu\nu}\mathcal{L} - (\mathcal{L}_X F_{\mu\sigma} + \mathcal{L}_Y^* F_{\mu\sigma}) F_{\nu}{}^{\sigma}]. \quad (4)$$

The Jacobi identities can be expressed as follows: $\nabla_{\mu}(*F^{\mu\nu}) = 0$. To introduce a Legendre dual description of the NLED theory, one involves the antisymmetric tensor $P_{\mu\nu}$ defined by $d\mathcal{L}(X, Y) = -\frac{1}{2}P^{\mu\nu}dF_{\mu\nu}$, $*F^{\mu\nu} = 0$ where $\mathcal{L}(X, Y)$ is the Lagrangian of the nonlinear electrodynamics (NLED) theory. The Lagrangian density for the Euler-Heisenberg nonlinear electrodynamics can be expressed in general as:

$$P^{\mu\nu} = 2\frac{\partial\mathcal{L}}{\partial F_{\mu\nu}} = -[\mathcal{L}_X F^{\mu\nu} + \mathcal{L}_Y^* F^{\mu\nu}] \quad (5)$$

with the field equation $\nabla_{\mu}P^{\mu\nu} = 0$. For the Euler-Heisenberg theory, the dual Plebanski tensor $P_{\mu\nu}$ is given by

$$P_{\mu\nu} = F_{\mu\nu} - \frac{4\alpha^2}{45m^4} (4X F_{\mu\nu} + 7Y^* F_{\mu\nu}). \quad (6)$$

The invariants of the tensor $P_{\mu\nu}$ can be expressed as

$$s = -\frac{1}{4}P_{\mu\nu}P^{\mu\nu}, \quad t = -\frac{1}{4}P_{\mu\nu}^*P^{\mu\nu}.$$

Here, $*P^{\mu\nu} = \frac{1}{2}\sqrt{-g}\epsilon^{\mu\nu\sigma\rho}P_{\sigma\rho}$. The structural function \mathcal{H} can be expressed as $\mathcal{H}(s, t) = -\frac{1}{2}P^{\mu\nu}F_{\mu\nu} - \mathcal{L}$. For the Euler-Heisenberg theory, the structural function \mathcal{H} (up to terms of higher order in α) is given by $H(s, t) = s - \frac{2\alpha^2}{45m^4}(4s^2 + 7t^2)$. The energy-momentum tensor of P is defined as $T_{\mu\nu} = \mathcal{H}_s P_{\mu\alpha}P_{\nu}{}^{\alpha} + g_{\mu\nu}(2s\mathcal{H}_s + t\mathcal{H}_t - \mathcal{H})$. It should be noted that the Maxwell linear electrodynamics is recovered when $F_{\mu\nu} = P_{\mu\nu}$. Then the energy-momentum tensor, written in the P frame, reads

$$T_{\mu\nu} = \frac{1}{4\pi} \left[\left(1 - \frac{16\alpha^2}{45m^4}X\right) F_{\mu}{}^{\beta}F_{\nu\beta} - \frac{28\alpha^2}{45m^4}Y (F_{\mu}{}^{\beta*}F_{\nu\beta} + *F_{\mu}{}^{\beta}F_{\nu\beta}) - g_{\mu\nu} \left(X - \frac{2\alpha^2}{45m^4}(4X^2 + 21Y^2)\right) \right]. \quad (7)$$

The energy-momentum tensor in terms of the dual variables reads

$$T_{\mu\nu} = \frac{1}{4\pi} \left[\left(1 - \frac{16\alpha^2}{45m^4}s\right) P_{\mu}{}^{\beta}P_{\nu\beta} + g_{\mu\nu} \left(s - \frac{2\alpha^2}{45m^4}(12s^2 + 7t^2)\right) \right]. \quad (8)$$

The relationship between $F_{\mu\nu}$ and $P_{\mu\nu}$ is:

$$F_{\mu\nu} = H_s P_{\mu\nu} + H_t^* P_{\mu\nu} = P_{\mu\nu} - \frac{16\alpha^2}{45m^4} \left[s P_{\mu\nu} + \frac{7}{4} t^* P_{\mu\nu} \right]. \quad (9)$$

Thus, assuming a Kerr-like spacetime with the Euler-Heisenberg nonlinear electrodynamics (NLED) as the source, the resulting spacetime resembles a screened Kerr-Newman solution. In Boyer-Lindquist coordinates, the potential describing the electromagnetic aspect of the EEH theory in terms of the dual Plebanski variables is determined by the ansatz

$$B = B_{\alpha}dx^{\alpha} = -\frac{Qa \cos\theta}{\Sigma} \left(dt - \frac{(r^2 + a^2)}{a} d\phi \right), \quad (10)$$

with the dual Plebanski 2-form

$$*P = dB^*P = \frac{2Q}{\Sigma^2} ar \cos\theta dr \wedge (dt - a \sin^2\theta d\phi) + \frac{Q}{\Sigma^2} (r^2 - a^2 \cos^2\theta) \sin\theta d\theta \wedge [adt - (r^2 + a^2) d\phi], \quad (11)$$

which satisfies the relations

$$*P_{r\phi} = a \sin^2\theta^*P_{tr}, \quad a^*P_{\theta\phi} = (r^2 + a^2)^*P_{t\theta}. \quad (12)$$

The Plebanski 2-form reads

$$P = \frac{Q}{\Sigma^2} (r^2 - a^2 \cos^2\theta) dr \wedge (dt - a \sin^2\theta d\phi) + \frac{Q}{\Sigma^2} ar \sin 2\theta d\theta \wedge [(r^2 + a^2) d\phi - adt]. \quad (13)$$

The components are also related by $P_{r\phi} = a \sin^2 \theta P_{tr}$ and $aP_{\theta\phi} = (r^2 + a^2) P_{t\theta}$. We obtain the invariants \tilde{s} and \tilde{t} as

$$\begin{aligned}\tilde{s} &= \frac{Q^2}{2\Sigma^2} - \frac{4\mathcal{M}^2 r^2 \cos^2 \theta}{\Sigma^4} \\ \tilde{t} &= \frac{2Qr \cos \theta}{\Sigma^4} \mathcal{M} (r^2 - a^2 \cos^2 \theta).\end{aligned}\quad (14)$$

Therefore, the solution for $A = A_\nu dx^\nu$ can be derived as follows

$$A = \left\{ 1 - \frac{10\alpha}{225\pi} D_Q^2 + \frac{10\alpha}{225\pi} H_Q^2 + \frac{60\alpha}{225\pi} H_Q^2 \frac{H_Q^2}{D_Q^2} \right\} \times \frac{Qr}{\Sigma} [dt - a \sin^2 \theta d\phi], \quad (15)$$

and

$$D_Q^2 = \frac{Q^2}{\Sigma^2 D_c^2}, \quad H_Q^2 = \frac{\mathcal{M}^2 \cos^2 \theta}{\Sigma^3 D_c^2}, \quad (16)$$

with $D_c = m_e^2 c^3 / (e\hbar)$ is the critical field. In the expression above, we utilized the relation $16\alpha^2 / (45m_e^4) = 20\alpha / (225\pi D_c^2)$. For $\alpha = 0$, gives the usual electromagnetic potential for the KN black hole solution is recovered.

Furthermore, the energy-momentum tensor $T^{\mu\nu}$ for the Euler-Heisenberg nonlinear electrodynamics (NLED) is given by

$$\begin{aligned}8\pi T^{rr} &= -\frac{\Delta Q^2}{\Sigma^3} \left(1 - \frac{16\alpha^2}{45m_e^4} \tilde{s} \right) - \frac{16\alpha^2}{45m_e^4} \frac{\Delta}{\Sigma} \left(\tilde{s}^2 + \frac{7}{4} \tilde{t}^2 \right), \\ 8\pi T^{\theta\theta} &= \frac{Q^2}{\Sigma^3} \left(1 - \frac{16\alpha^2}{45m_e^4} \tilde{s} \right) - \frac{16\alpha^2}{45m_e^4} \frac{1}{\Sigma} \left(\tilde{s}^2 + \frac{7}{4} \tilde{t}^2 \right), \\ T^{tt} &= -\frac{(r^2 + a^2)^2}{\Delta^2} T^{rr} + a^2 \sin^2 \theta T^{\theta\theta}, \\ T^{t\phi} &= -\frac{(r^2 + a^2) a}{\Delta^2} T^{rr} + a T^{\theta\theta}, \\ T^{\phi\phi} &= -\frac{a^2}{\Delta^2} T^{rr} + \frac{1}{\sin^2 \theta} T^{\theta\theta}.\end{aligned}\quad (17)$$

Hence, we obtain the rotating spherically symmetric metric of EEH black hole spacetime [24, 25, 58]

$$\begin{aligned}ds^2 &= - \left(1 - \frac{2Mr - \tilde{Q}^2}{\rho^2} \right) dt^2 + \frac{\rho^2}{\Delta} dr^2 - \frac{(2Mr - \tilde{Q}^2) 2a \sin^2 \theta}{\rho^2} dt d\phi + \rho^2 d\theta^2 \\ &+ \left[r^2 + a^2 + \frac{(2Mr - \tilde{Q}^2) a^2 \sin^2 \theta}{\rho^2} \right] \sin^2 \theta d\phi^2,\end{aligned}\quad (18)$$

where

$$\rho^2 = r^2 + a^2 \cos^2 \theta, \quad \Delta = r^2 + a^2 - 2Mr + \tilde{Q}^2, \quad (19)$$

which represents a screened KN-like black hole. The screened charge of the black hole is defined as

$$\tilde{Q}^2 = Q^2 \left\{ 1 - \frac{5\alpha}{225\pi} \left[D_Q^2 - 4H_Q^2 \left(1 - \frac{a^2 \cos^2 \theta}{\Sigma} \right) \times \left(7 - 12 \frac{a^2 \cos^2 \theta}{\Sigma} + 12 \frac{a^4 \cos^4 \theta}{\Sigma^2} \right) \right] \right\}. \quad (20)$$

The main metric reads

$$\begin{aligned}ds^2 &= - \left(1 - \frac{2Mr - Q_e^2 + A Q_e^4 / 20r^4}{\rho^2} \right) dt^2 + \frac{\rho^2}{\Delta} dr^2 - \frac{4a \left(Mr - \frac{Q_e^2}{2} + A Q_e^4 / 40r^4 \right) \sin^2 \theta}{\rho^2} dt d\phi \\ &+ \rho^2 d\theta^2 + \frac{\Sigma \sin^2 \theta}{\rho^2} d\phi^2,\end{aligned}\quad (21)$$

where

$$\begin{aligned}\rho^2 &= r^2 + a^2 \cos^2 \theta, \\ \Delta &= r^2 + a^2 - 2m(r)r, \\ \Sigma &= (r^2 + a^2)^2 - a^2 \Delta \sin^2 \theta,\end{aligned}\tag{22}$$

and

$$m(r) = M - \frac{Q_e^2}{2r} + A \frac{Q_e^4}{40r^5}.\tag{23}$$

We have reduced the EEH rotating black hole solution to a Kerr-Newman-like black hole one. By setting $a = 0$, the static screened Reissner-Nordstrom solution is recovered. In order to gain some physical insight into the energy-mass function, we could allow to vary from point to point in the spacetime. In this framework, the solution behaves asymptotically as the Kerr-Newman one.

III. NULL REGIONS

Recall that in the Kerr case, it is well-known that if the spin parameter is extremal ($a = M$), two horizons coincide at $r = M$. It means that the minima of the curve by the function $\Delta(r)$ coincides $r = M$ at $\Delta(r) = 0$. If $a = 0$, we expect the Schwarzschild case for the horizon where $r = 2M$. For the Reissner-Nordstrom case, two horizons are also formed due to the effect of the black hole charge Q_e . Similar to the Kerr case, the critical value for the charge is $Q_e = M$. Any charge greater than M would produce an imaginary horizon and unphysical. In the Kerr-Newman (KN) case, it can be shown that the critical value of charge for the horizons to be physical is $Q_e = \sqrt{M^2 - a^2}$. It implies that as a tends to be large, Q_e should have a small value.

For the EEH black hole, we have the KN case with the addition of the screening parameter A . Thus, it is meaningful to explore the effect A on the critical value of the black hole charge given a . We numerically show this in Fig. 1, where we include the Kerr and the KN case for comparison ($a = 0.90M$). Interestingly, there are two different results as we consider the different signs of A . When A becomes increasingly negative, the minima deviates farther from $\Delta(r) = 0$, which implies that one needs a value of Q_e that is lower relative to the critical value in the KN case ($Q_e \sim 0.436M$). When A becomes increasingly positive, the Cauchy horizon disappears, and only the event horizon remains. We observe that the radius of the event horizon approaches the horizon of the non-rotating case as A continues to get large.

In the right panel of Fig. 1, we explored the effect of decreasing the value of Q_e , which is noticeable for the Kerr and KN cases. We observed in this case that the horizon shifts closer to $a = M$ when A becomes less positive. However, it turns out that A being negative needs a small amount of black hole charge Q_e for the Cauchy and event horizon to manifest. Indeed, the positive value of A has a vanishing effect on the Cauchy horizon, while the negative value of A has a vanishing effect for both, unless the black hole charge is very small.

Next, we examined the ergosphere radii. For the KN case, the critical value of charge must be $Q_e = \sqrt{M^2 - a^2 \cos^2(\theta)}$. The numerical plot is shown in Fig. 2. At $\theta = \pi/2$ (left panel), this is the same as the critical value for the horizon. As A becomes increasingly negative, one needs a smaller value of Q_e for the physical manifestation of the ergosphere to occur. By contrast, we observe only one ergosphere radius occurring in this critical value of Q_e , getting closer to $r = 2M$ as A becomes more positively large. In the right panel, we considered $\theta = \pi/4$, and with Q_e that is less than the critical value. We observe that positive values of A have a negligible effect on the outer ergosphere and remove the inner ergosphere. In contrast, negative values of A introduce a larger value of the inner ergoregion as compared to the Kerr and KN cases. It is also interesting to note that for $A = -1000$, the ergosphere exists even if there is no inner and outer horizon present.

IV. NULL GEODESICS

In this section, we start with the analysis of photon geodesic by utilizing the Hamilton-Jacobi equation, which gives

$$\frac{\partial S}{\partial \lambda} = -H,\tag{24}$$

where S is the Jacobi action, λ is the proper time (or the affine parameter). In terms of the coordinate x_μ , the Hamiltonian in General Relativity is given by

$$H = \frac{1}{2} g^{\mu\nu} \frac{\partial S(\lambda)}{\partial x^\mu} \frac{\partial S}{\partial x^\nu},\tag{25}$$

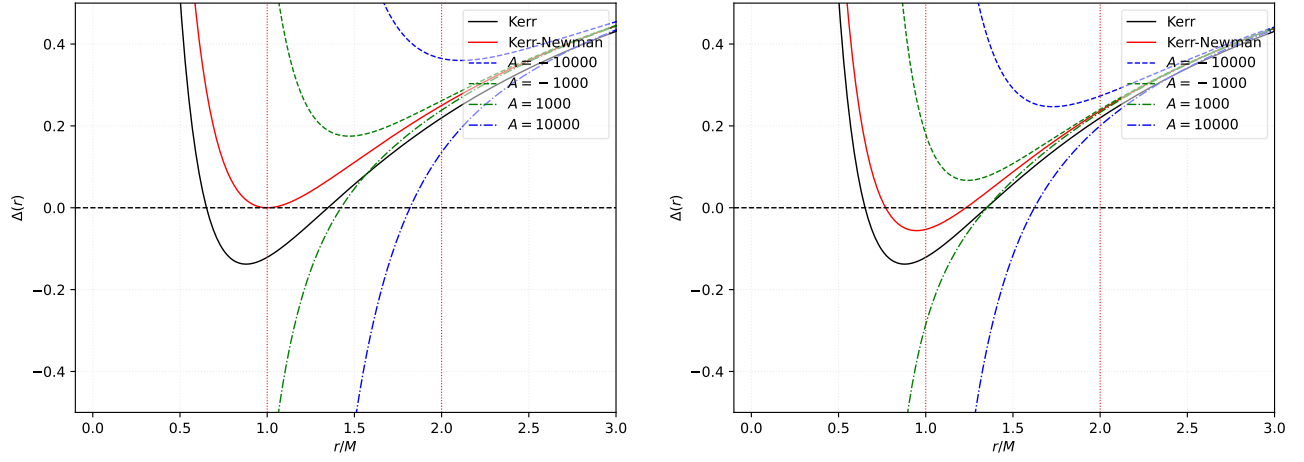


FIG. 1. Behavior of the event horizon. Left panel: $Q_e \sim 0.348M$, which is the critical value of charge in the KN case. Right panel: $Q_e \sim 0.261M$. In these plots, we assumed $a = 0.9375M$. The red dotted vertical line represents the horizon radius when $a = 0$ and $a = M$.

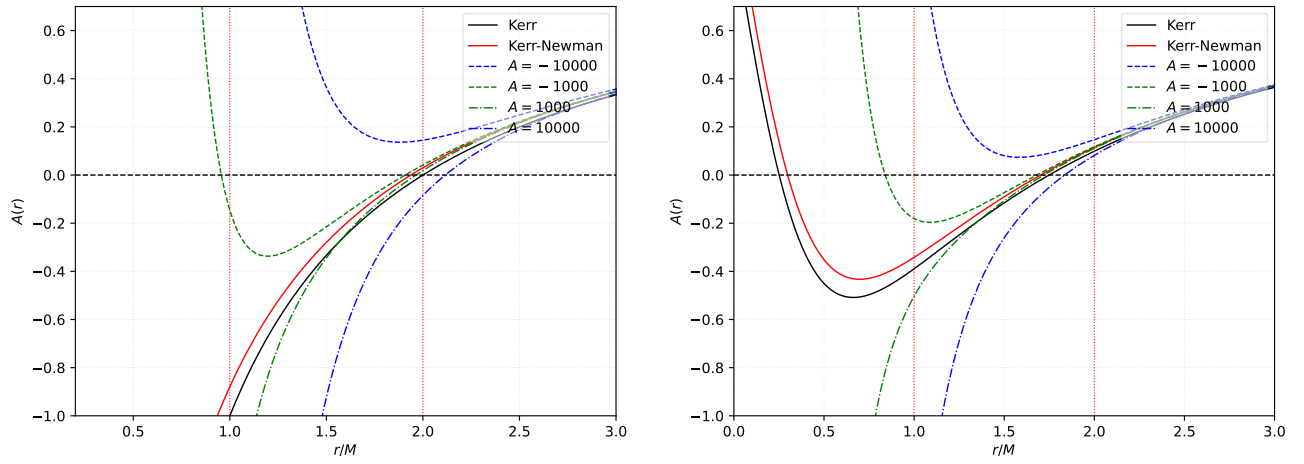


FIG. 2. Behavior of the ergo region. Left panel: $\theta = \pi/2$, where $Q_e \sim 0.348M$. Right panel: $\theta = \pi/4$, where $Q_e \sim 0.261M$. In these plots, we assumed $a = 0.90M$. The red dotted vertical line represents the horizon radius when $a = 0$ and $a = M$.

so that

$$\frac{\partial S}{\partial \lambda} = -\frac{1}{2}g^{\mu\nu} \frac{\partial S}{\partial x^\mu} \frac{\partial S}{\partial x^\nu}, \quad (26)$$

as follows from Eq. (24) above. Let's use the separability ansatz for the Jacobi function

$$S = \frac{1}{2}\mu^2\lambda - Et + L\phi + S_r(r) + S_\theta(\theta), \quad (27)$$

and with the particle mass μ , one can obtain the following first-order motion equations [59]

$$\begin{aligned} \Sigma \frac{dt}{d\lambda} &= \frac{\Xi(r^2 + a^2)P(r)}{\Delta_r} - \frac{\Xi a P(\theta)}{\Delta_\theta}, \\ \Sigma \frac{dr}{d\lambda} &= \sqrt{R(r)}, \\ \Sigma \frac{d\theta}{d\lambda} &= \sqrt{\Theta(\theta)}, \end{aligned}$$

$$\Sigma \frac{d\phi}{d\lambda} = \frac{\Xi a P(r)}{\Delta_r} - \frac{\Xi P(\theta)}{\Delta_\theta \sin^2 \theta}, \quad (28)$$

where

$$\begin{aligned} R(r) &= P(r)^2 - \Delta_r(\mu^2 r^2 + K), \\ P(r) &= \Xi E(r^2 + a^2) - \Xi a L, \\ \Theta(\theta) &= \Delta_\theta(K - \mu^2 a^2 \cos^2 \theta) - \frac{P(\theta)^2}{\sin^2 \theta}, \\ P(\theta) &= \Xi(aE \sin^2 \theta - L). \end{aligned} \quad (29)$$

The consequence of a hidden symmetry in the θ -coordinate [59, 60] gives a constant of motion $K = \Xi^2(aE - L)^2$, found in the third equation in Eq. (29) above

The geodesic of massless particles can be easily studied by setting $\mu = 0$. In determining the unstable circular orbit of photons, the condition below must be satisfied:

$$R(r) = \left. \frac{dR(r)}{dr} \right|_{r=r_{\text{ps}}} = 0. \quad (30)$$

The photon-sphere region is deeply related to the shadow cast by a black hole. A small perturbation on the orbit may cause photons to escape from r_{ps} to infinity, and then reach the observer's detectors. This is called backward ray tracing. For photons, it is always useful to define two impact parameters:

$$\xi = \frac{L}{E} \quad \text{and} \quad \eta = \frac{K}{E^2}. \quad (31)$$

The former is the impact parameter associated to the ϕ coordinate, while the latter is to the θ coordinate, which is a generalization to include latitudinal motion contribution of photons. Using the function $R(r)$ in Eq. (29) and the condition present in Eq. (30), the above quantities are given explicitly by

$$\begin{aligned} \xi &= \frac{\Delta'_r(r^2 + a^2) - 4\Delta_r r}{a\Delta'_r}, \\ \eta &= \frac{-r^4 \Delta_r'^2 + 8r^3 \Delta_r \Delta_r' + 16r^2 \Delta_r(a^2 - \Delta_r)}{a^2 \Delta_r'^2}, \end{aligned} \quad (32)$$

which is a convenient expression due to the fact that it can describe any black hole model described by the function Δ_r . Depending on how complicated Δ_r is, analytic or numerical values of r_{ps} can be sought off by solving r in $\eta = 0$. The analytical solutions are well-known for both Schwarzschild and Kerr black holes (which have two values for r_{ps}). The plot is shown in Fig. 3 for three cases: retrograde, prograde, and the orbit that defines zero angular momentum. For a given spin parameter, we see in the inset plot on the left panel how different signs of the screening parameter cause deviation from the KN case. Same can be concluded with the right panel, with the only difference that the negative screening parameter produces only one outer orbit.

V. SHADOW CAST AND OBSERVABLES

As mentioned earlier, escaping photons define the shadow cast and it can be done by using the celestial coordinates of the observer at (r_o, θ_o) . Such an observer is also known as the Zero Angular Momentum Observer (ZAMO). The general definition of the celestial coordinates is [61]

$$\begin{aligned} \alpha &= -r_o \frac{\xi}{\zeta \sqrt{g_{\phi\phi}} \left(1 + \frac{g_{t\phi}}{g_{\phi\phi}} \xi\right)}, \\ \beta &= r_o \frac{\pm \sqrt{\Theta(\theta_o)}}{\zeta \sqrt{g_{\theta\theta}} \left(1 + \frac{g_{t\phi}}{g_{\phi\phi}} \xi\right)}, \end{aligned} \quad (33)$$

and the condition $r_o \rightarrow \infty$ leads to the simplified relations

$$\alpha = -\xi \csc \theta_o,$$

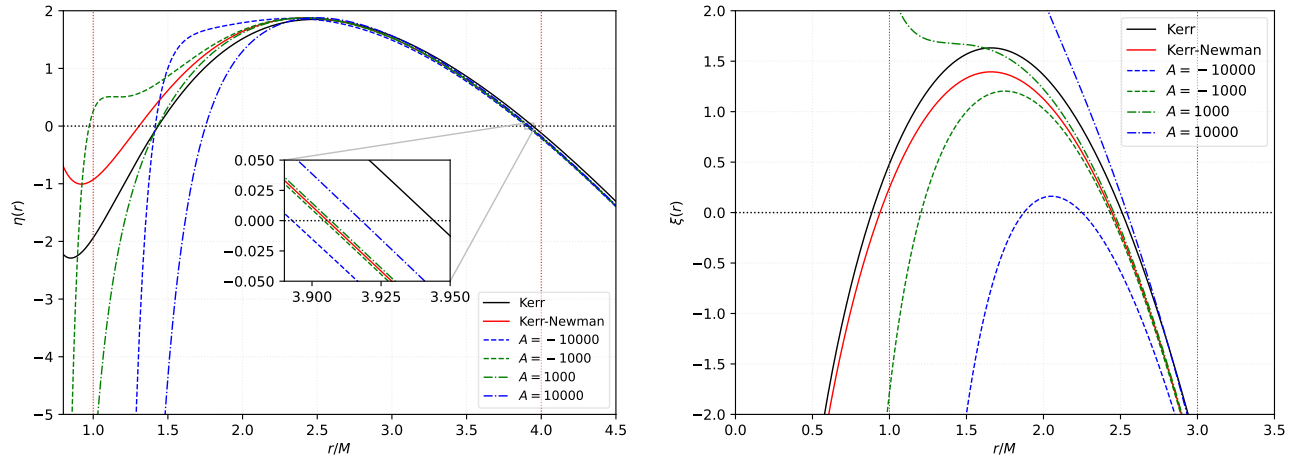


FIG. 3. Left panel: retrograde and prograde photons. Right panel: zero angular momentum orbit. Here, $a = 0.9375M$ and $Q_e = 0.246M$

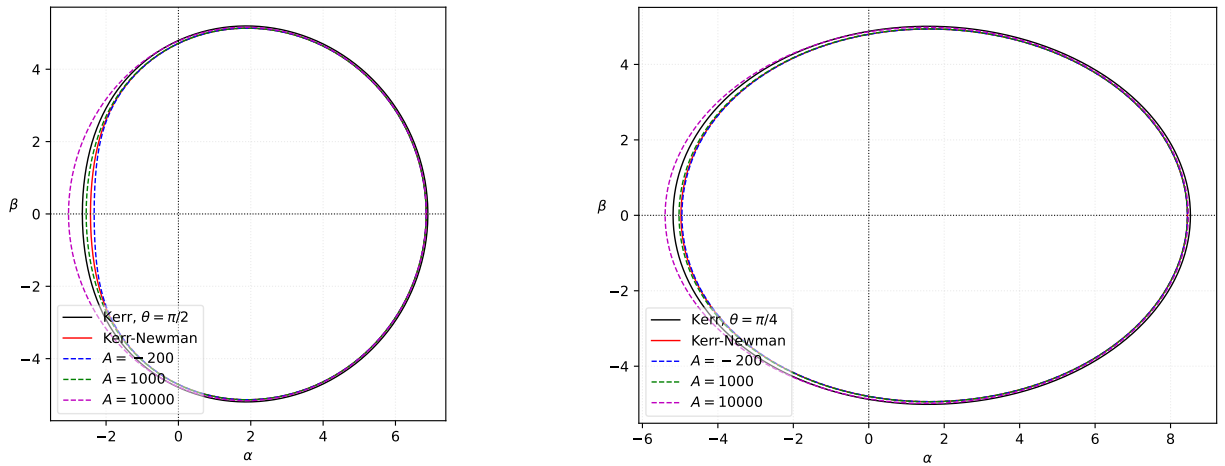


FIG. 4. Left panel: Case of different screening parameters at inclination $\theta = \pi/2$, where $Q_e = 0.261M$ and $a = 0.9375M$. Right panel: Case of different screening parameters at inclination $\theta = \pi/4$.

$$\beta = \pm \sqrt{\eta + a^2 \cos^2 \theta_o - \xi^2 \cot^2 \theta_o}. \quad (34)$$

If the observer is at the equatorial plane $\theta_o = \pi/2$, these expressions reduce to $\alpha = 0$ and $\beta = \pm \sqrt{\eta}$. Furthermore, when $a = 0$, we obtain the shadow cast as a perfect circle. The plot of β vs. α is shown in Fig. 4 for the black hole spin parameter value of $a = 0.9375M$. We added the Kerr and the KN cases for comparison.

Due to the high spin that we considered, the D-shaped nature of the shadow cast manifests clearly for the Kerr case. Relative to this, the D-shape is more pronounced for the KN case as we add the charge Q_e . For the effect of the screening parameter, a negative value amplifies the effect of the KN case, but the positive value tends to remove the D-shaped feature as the parameter increases. We can also observe that the behavior of the photon-sphere under the effect of the screening parameter is the same as the shadow cast. Finally, when the observer's polar position changes, the shadow becomes more oblate.

As the spin parameter a becomes more extremal, one can still obtain the shadow radius defined by R_{sh} . Its numerical value can be calculated via [62, 63]

$$R_{\text{sh}} = \frac{\beta_t^2 + (\alpha_t - \alpha_r)^2}{2|\alpha_t - \alpha_r|}. \quad (35)$$

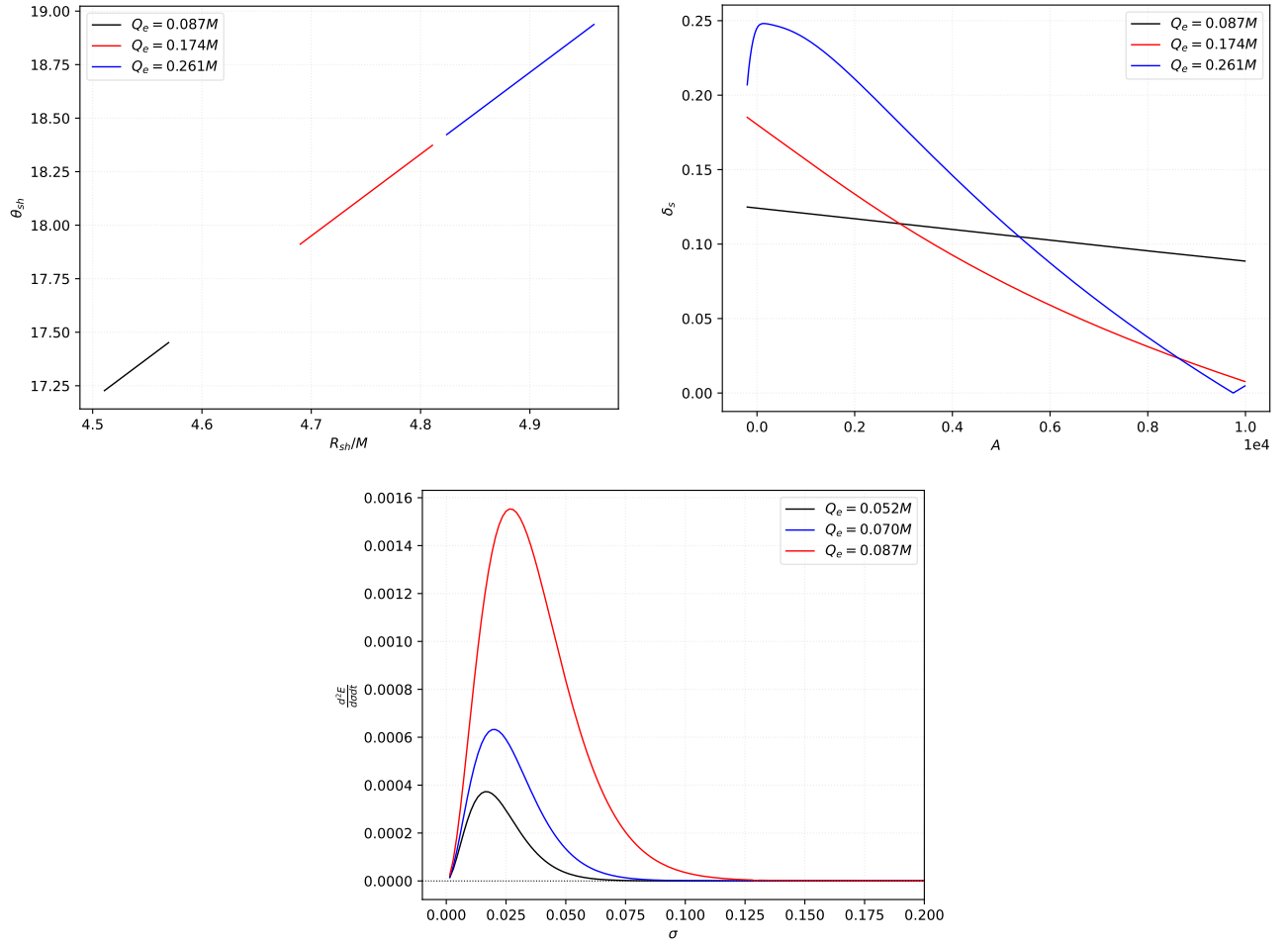


FIG. 5. Upper left panel: Angular radius using the mass of M87* and our actual distance. Upper right panel: Behavior of the distortion parameter as A varies for different Q_e . Lower panel: The energy emission rate as frequency σ varies for different Q_e (Note that this is also for varying A). In all these plots, $a = 0.90M$.

Using the above equation, we can define the shadow's angular radius θ_{sh} :

$$\theta_{sh} = 9.87098 \times 10^{-3} \frac{R_{sh}M}{D}, \quad (36)$$

where M is the black hole's mass in units of M_{\odot} , and D is measured in parsec. We plot the numerical result in Fig. 5 at the upper left panel, which is consistent with Fig. 4. Other observables that can be derived from the shadow are the distortion parameter δ_{sh} and the energy emission rate $\frac{d^2E}{d\omega dt}$, which are defined as follows:

$$\delta_{sh} = \frac{d_{sh}}{R_{sh}} = \frac{\tilde{\alpha}_1 - \alpha_1}{R_{sh}}, \quad (37)$$

$$\frac{d^2E}{d\omega dt} = 2\pi^2 \frac{\Pi_{ilm}}{e^{\omega/T} - 1} \omega^3. \quad (38)$$

We can approximate the energy absorption cross-section as $\Pi_{ilm} \sim \pi R_{sh}^2$ for an observer at $r_o \rightarrow \infty$. We plot these two observables in Fig. 5 upper right panel and lower panel, where we can see how these observables behave due to the effect of the black hole charge Q_e and the screening parameter. As for the energy emission rate, as it is related to the black hole's lifetime, higher Q_e makes the EEH black hole emit more energy. Also, we observe that peak frequency shifts to higher values as Q_e increases.

VI. QNMS USING WKB APPROXIMATION

This section deals with the QNMs of both the rotating and static black holes by using WKB approximation methods. QNMs, which characterize the damped oscillations of perturbations in the black hole spacetime, provide critical insights into the stability and properties of these celestial objects. The WKB (Wentzel - Kramers - Brillouin) approximation method, known for its effectiveness in semi-classical analyses, is employed to derive and analyze the frequencies and damping rates of these oscillations. By applying this method, we aim to elucidate the differences and similarities in the QNM spectra of rotating versus static black holes, thereby enhancing our understanding of their dynamic behaviours under perturbations.

A. The rotating case

In this subsection, we shall derive equations representing the frequencies of QNMs associated with this rotating black hole using the WKB approximation. This requires determining both the real and imaginary components of ω with leading and next-to-leading order accuracy. Our focus will be on obtaining an analytical approximation for the frequency spectrum corresponding to this black hole solution. Although higher-order WKB methods are more reliable, in the case of rotating black holes, due to the complexity of the method, we shall use the WKB method only up to the leading order corrections.

Before we delve into the specifics of our results pertaining to the angular and radial Teukolsky equations, it is essential to revisit a fundamental aspect of the WKB expansion. This concept will be a recurring theme throughout our paper. For a more comprehensive discussion of WKB methods, please refer to [64–70].

In the beginning, we consider a wave equation for the wave function $\psi(x)$, given by:

$$\epsilon^2 \frac{d^2 \psi}{dx^2} + U(x)\psi = 0. \quad (39)$$

In the above equation, ϵ is a small positive number. For this equation, the solution can be expanded in the following form:

$$\psi = e^{\frac{S_0}{\epsilon} + S_1 + \epsilon S_2 + \dots}. \quad (40)$$

In the above expansion, the primary and secondary variables *i.e.*, S_0 and S_1 can be expressed in the following form [70]:

$$S_0 = \pm i \int^x \sqrt{U(x)} dx, \quad (41a)$$

$$S_1 = -\frac{1}{4} \log U(x). \quad (41b)$$

These formulas will serve as the foundation for our examination of the radial and angular Teukolsky equations in the subsequent parts of our study.

Teukolsky demonstrated that the Kerr spacetime's scalar, vector, and tensor perturbations all adhere to a unified master equation for scalar variables with spin weight \bar{s} . Furthermore, this master equation can be solved through a separation of variables approach [71]. We will employ the variable u to represent our scalar field, and we shall decompose this scalar wave as follows [70, 72, 73]:

$$u(t, r, \theta, \phi) = e^{-i\omega t} e^{im_l \phi} u_r(r) u_\theta(\theta). \quad (42)$$

Subsequently, at the relevant order for $l \gg 1$, the angular equation for $u_\theta(\theta)$ can be expressed as:

$$\frac{1}{\sin \theta} \frac{d}{d\theta} \left[\sin \theta \frac{du_\theta}{d\theta} \right] + \left[a^2 \omega^2 \cos^2 \theta - \frac{m_l^2}{\sin^2 \theta} + \mathcal{A}_{lm_l} \right] u_\theta = 0, \quad (43)$$

where \mathcal{A}_{lm_l} represents the angular eigenvalue of this equation. The equation governing the radial function $u_r(r)$ is given by:

$$\frac{d^2 u_r}{dr_*^2} + \frac{K^2 - \Delta \lambda_{lm_l}^0}{(r^2 + a^2)^2} u_r = 0, \quad (44)$$

with the definitions of the parameters as follows:

$$K = -\omega(r^2 + a^2) + am_l, \quad (45)$$

$$\lambda_{lm_l}^0 = \mathcal{A}_{lm_l} + a^2\omega^2 - 2am_l\omega. \quad (46)$$

It is worth noting that in our calculations, we have neglected higher-order terms based on the facts that $\omega_R \sim O(l)$, $\omega_I \sim O(1)$, and $m_l \sim O(l)$ in comparison to the terms we are considering. Therefore, the spin parameter associated with the perturbation has no impact on the equations governing QNMs of the black hole spacetime. In the above equation governing the behaviour of the radial function u_r , the rate of variation is calculated with respect to the tortoise coordinate r_* which is defined as,

$$\frac{d}{dr_*} \equiv \frac{\Delta}{r^2 + a^2} \frac{d}{dr}$$

We can derive an expression for \mathcal{A}_{lm_l} in terms of ω , l , and m_l by analyzing the angular equation within the WKB approximation. To begin, let us outline our approach to this calculation. Given that the frequency $\omega = \omega_R - i\omega_I$ is complex, the angular eigenvalue \mathcal{A}_{lm_l} , which depends on ω , must also be complex [70, 73]. We express this as:

$$\mathcal{A}_{lm_l} = A_{lm}^R + iA_{lm}^I, \quad (47)$$

to distinguish between the real and imaginary components. By utilizing perturbation theory for eigenvalue equations, we find:

$$\mathcal{A}_{lm_l}^I = -2a^2\omega_R\omega_I \langle \cos^2 \theta \rangle, \quad (48)$$

where the expectation value is given by the following expression:

$$\begin{aligned} \langle \cos^2 \theta \rangle &= \frac{\int \cos^2 \theta |u_\theta|^2 \sin \theta d\theta}{\int |u_\theta|^2 \sin \theta d\theta} \\ &= \frac{\int_{\theta_-}^{\theta_+} \frac{\cos^2 \theta}{\sqrt{a^2\omega_R^2 \cos^2 \theta - \frac{m_l^2}{\sin^2 \theta} + \mathcal{A}_{lm_l}^R}} d\theta}{\int_{\theta_-}^{\theta_+} \frac{1}{\sqrt{a^2\omega_R^2 \cos^2 \theta - \frac{m_l^2}{\sin^2 \theta} + \mathcal{A}_{lm_l}^R}} d\theta}. \end{aligned} \quad (49)$$

The Bohr-Sommerfeld condition for such a case from Ref. [70] can be given as

$$\int_{\theta_-}^{\theta_+} d\theta \sqrt{a^2\omega_R^2 \cos^2 \theta - \frac{m_l^2}{\sin^2 \theta} + \mathcal{A}_{lm_l}^R} = (l + 1/2 - |m_l|) \pi. \quad (50)$$

By differentiating the Bohr-Sommerfeld condition (50) with respect to the variable $z = a\omega_R$ and considering the parameter \mathcal{A}_{lm_l} as a function of z , we can reformulate the expression as follows:

$$\langle \cos^2 \theta \rangle = -\frac{1}{2z} \left. \frac{\partial \mathcal{A}_{lm_l}^R(z)}{\partial z} \right|_{z=a\omega_R}. \quad (51)$$

We use this expression into the Eq. (48) to obtain the following relation

$$\mathcal{A}_{lm_l}^I = a\omega_I \left[\frac{\partial \mathcal{A}_{lm_l}^R(z)}{\partial z} \right]_{z=a\omega_R}. \quad (52)$$

This Eq. (52) outlines a numerical method for determining $\mathcal{A}_{lm_l} = \mathcal{A}_{lm_l}^R + i\mathcal{A}_{lm_l}^I$ for a rotating black hole. As expected, the term is a complex quantity. The real part of it is associated with the oscillation frequency of ring-down GWs. An approximation of this relation gives us,

$$\mathcal{A}_{lm_l} \approx (l + 1/2)^2 - \frac{a^2\omega^2}{2} \left[1 - \frac{m_l^2}{(l + 1/2)^2} \right]. \quad (53)$$

After calculating the angular eigenvalues \mathcal{A}_{lm_l} in terms of the oscillation frequency ω , we turn our focus to the radial Teukolsky equation. As shown in Eq. (44), the radial equation is formulated as:

$$\frac{d^2 u_r}{dr_*^2} + V^r u_r = 0, \quad (54)$$

where the potential associated with the above equation can be expressed as

$$V^r(r, \omega) = \frac{[\omega(r^2 + a^2) - m_l a]^2 - \Delta [\mathcal{A}_{lm_l}(a\omega) + a^2\omega^2 - 2m_l a\omega]}{(r^2 + a^2)^2}. \quad (55)$$

Following Ref. [70], the leading-order WKB approximant for u_r can be expressed as:

$$u_r = b_+ e^{i \int^{r_*} \sqrt{V^r(r'_*)} dr'_*} + b_- e^{-i \int^{r_*} \sqrt{V^r(r'_*)} dr'_*}. \quad (56)$$

The outgoing mode $r_* \rightarrow +\infty$ and the ongoing mode $r_* \rightarrow -\infty$ demands that

$$u_r = b_+ e^{i \int^{r_*} \sqrt{V^r(r'_*)} dr'_*} \quad (57)$$

for the region having $r \rightarrow +\infty$, and

$$u_r = b_- e^{-i \int^{r_*} \sqrt{V^r(r'_*)} dr'_*} \quad (58)$$

for the region having $r_* \rightarrow -\infty$. In simpler terms, a solution to Eq. (54) will exhibit the specified asymptotic behavior if $V^r \approx 0$ at a point $r = r_0$, with V^r being positive on both sides of this point. This allows the WKB expansion (56) to be applied in the regions flanking $r = r_0$. However, the solution near r_0 must be determined separately and matched with the WKB approximation to constrain the frequency and thereby determine ω [70]. Iyer and Will performed an extensive calculation of this procedure to high orders in the WKB approximation. The main difference between their calculation and ours at lower orders is due to the more complex dependence of V^r on ω in our case, especially because \mathcal{A}_{lm_l} depends on ω in a more intricate manner. As stated in Ref. [64], the conditions that need to be solved at the leading and next-to-leading orders to determine ω_R are:

$$V^r(r_0, \omega_R) = \left. \frac{\partial V^r}{\partial r} \right|_{(r_0, \omega_R)} = 0. \quad (59)$$

Further, it is possible to write these conditions as:

$$\Omega_R = \frac{\mu a}{r_0^2 + a^2} \pm \frac{\sqrt{\Delta(r_0)}}{r_0^2 + a^2} \beta(a\Omega_R), \quad (60)$$

$$0 = \left. \frac{\partial}{\partial r} \left[\frac{\Omega_R(r^2 + a^2) - \mu a}{\sqrt{\Delta(r)}} \right] \right|_{r=r_0}, \quad (61)$$

where $\Omega_R = (l + 1/2)\omega_R$ and $\beta(a\Omega_R) = \sqrt{\frac{1}{2}a\Omega_R(a(\mu^2 + 1)\Omega_R - 4\mu) + 1}$. From (61) condition, one gets

$$\omega_R = \frac{am_l (AQ_e^4 + 10r_0^5 (r_0 - M))}{(a^2 (AQ_e^4 - 10r_0^5 (M + r_0)) + 2r_0^2 (AQ_e^4 - 5r_0^4 (-3Mr_0 + 2Q_e^2 + r_0^2)))} \quad (62)$$

The imaginary part ω_I can be calculated in the leading order using the method described by Iyer and Will in their work [64]. This approach yields the result that:

$$\omega_I = -(n + 1/2) \frac{\sqrt{2 \left(\frac{d^2 V^r}{dr_*^2} \right)_{r_0, \omega_R}}}{\left(\frac{\partial V^r}{\partial \omega} \right)_{r_0, \omega_R}}. \quad (63)$$

This expression shows that the leading order imaginary part ω_I depends on the overtone number n and is proportional to the square root of the second derivative of the potential with respect to the tortoise coordinate. Although this relation does not provide imaginary QNMs or damping rate of ring-down GWs up to the desired accuracy to compare with the observational results, it is still possible to theoretically understand the behavior of the ring-down modes by using this relation. In the case of rotating black holes, the higher-order corrections become too complex and hence we have limited our investigation to the leading orders only. For our case, the above relation, under a suitable approximation of the angular eigenvalues, gives

$$\omega_I = - \frac{(2l + 1)^3 (2n + 1) (20r_0^4 (a^2 - 2Mr_0 + Q_e^2 + r_0^2) - AQ_e^4) \sqrt{\frac{8\omega_R^2 (a^2 (12l(l+1) - 4m_l^2 + 3) + 12(2l+1)^2 r_0^2)}{(2l+1)^4} - 4}}{4\omega_R (C_1 + 20r_0^4 C_2) - 8a(2l + 1)^2 m_l (AQ_e^4 + 40Mr_0^5 - 20Q_e^2 r_0^4)}, \quad (64)$$

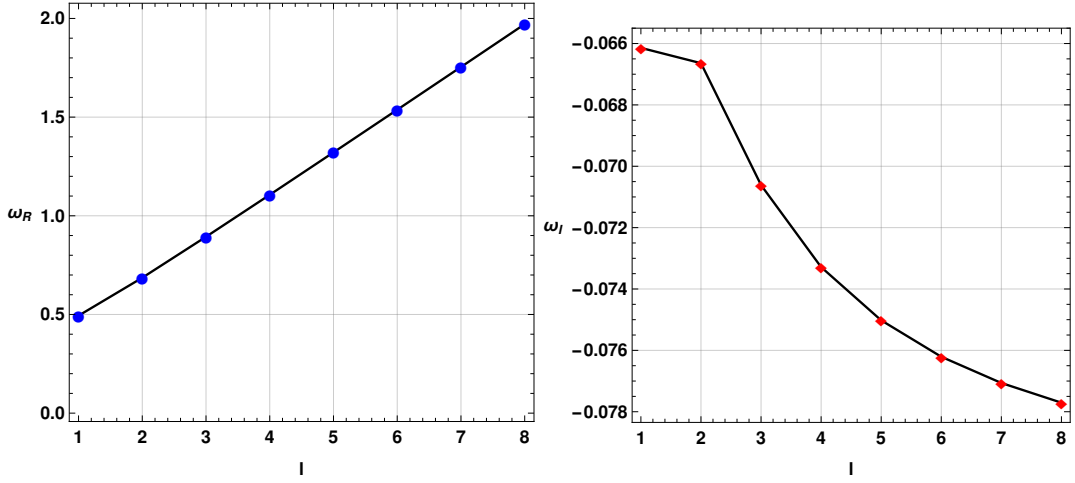


FIG. 6. Variation of real and imaginary QNMs using $M = 1, Q_e = 0.5, A = 100, a = 0.9, n = 0$ and $m_l = 1$.

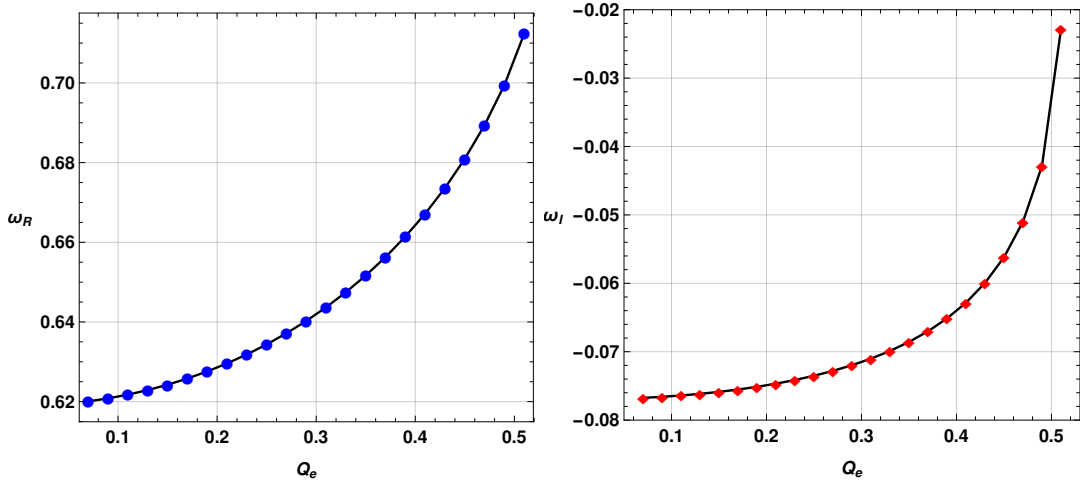


FIG. 7. Variation of real and imaginary QNMs using $M = 1, A = 10, a = 0.9, n = 0, l = 2$ and $m_l = 1$.

where

$$C_1 = a^2 A Q_e^4 ((2l+1)^2 + 4m_l^2), \quad (65)$$

$$C_2 = a^4 ((2l+1)^2 - 4m_l^2) + 2a^2 M r_0 ((2l+1)^2 + 4m_l^2) - a^2 Q_e^2 [(2l+1)^2 + 4m_l^2] + a^2 r_0^2 (12l(l+1) - 4m_l^2 + 3) + 2(2l+1)^2 r_0^4. \quad (66)$$

We have plotted the variation of QNMs for different values of multipole moments l in Fig. 6 using the above relations. In Fig. 7, we have shown how the QNMs vary with respect to the charge of the black hole Q_e . One may note that the real QNMs increase non-linearly with the value of Q_e . On the other hand, the damping rate of GWs decreases non-linearly with an increase in Q_e . With an increase in the parameter A , the oscillation frequency of ring-down GWs decreases, and the damping rate increases, as shown in Fig. 8. Finally, from Fig. 9, it is clear that for a rotating black hole, the oscillation frequency of ring-down GWs increases, and the damping rate decreases. The variation of damping rate or decay rate of ring-down GWs, as seen from the figure, is non-linear with respect to the parameter a . However, if we compare it with the Fig. 7, the charge parameter Q_e has a more significant impact on the damping rate than that of the parameter a .

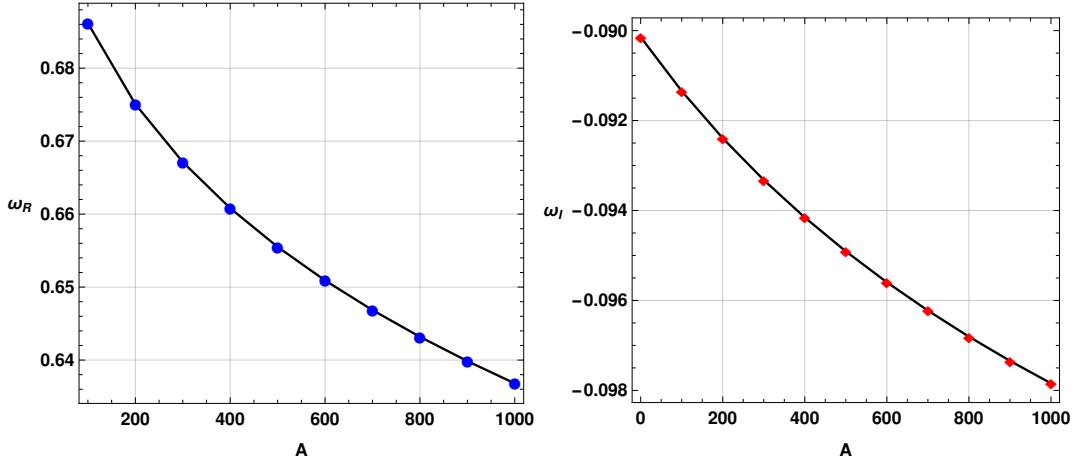


FIG. 8. Variation of real and imaginary QNMs using $M = 1, Q_e = 0.5, a = 0.9, n = 0, l = 2$ and $m_l = 1$.

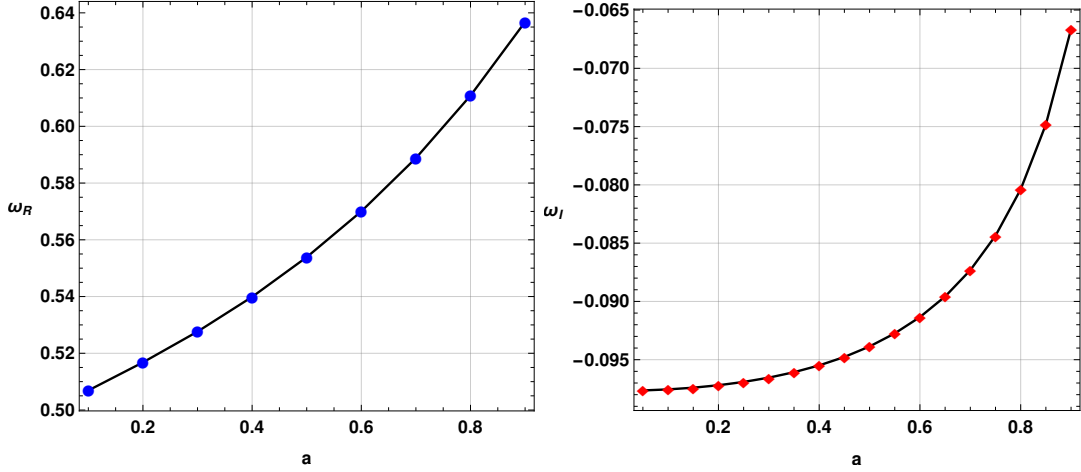


FIG. 9. Variation of real and imaginary QNMs using $M = 1, Q_e = 0.5, A = 100, n = 0, l = 2$ and $m_l = 1$.

B. Static case

In this part, we have calculated the QNMs of the black hole using $a = 0$ *i.e.*, static case. In this scenario, the scalar potential associated with the black hole becomes:

$$V_s(r) = \left(1 - \frac{2M}{r} + \frac{Q_e^2}{r^2} - \frac{AQ_e^4}{20r^6}\right) \left(\frac{3AQ_e^4}{10r^8} + \frac{2M}{r^3} - \frac{2Q_e^2}{r^4} + \frac{l(l+1)}{r^2}\right). \quad (67)$$

We have shown the variation of the potential in Fig. 10 for different values of multipole moment l , the model parameter A , and charge Q_e . With an increase in the value of A , the peak value of the potential decreases and shifts towards higher values of r . On the other hand, with an increase in the charge parameter Q_e , the peak value of the potential increases and shifts slightly towards higher values of r . Since the potential behaviour depends significantly on the model parameters, it suggests that the model parameters may have noticeable impacts on the QNMs spectrum of the black hole. Moreover, the WKB method deals with the maximum potential and from this perspective, it seems that the model parameters A and Q might have opposite impacts on the ring-down GWs.

For the static black hole case, we have used the 6th order Padé averaged WKB method to calculate the QNMs using the following expression [66, 67]:

$$\omega = \sqrt{-i \left[(n + 1/2) + \sum_{k=2}^6 \bar{\Lambda}_k \right] \sqrt{-2V_0''} + V_0}, \quad (68)$$

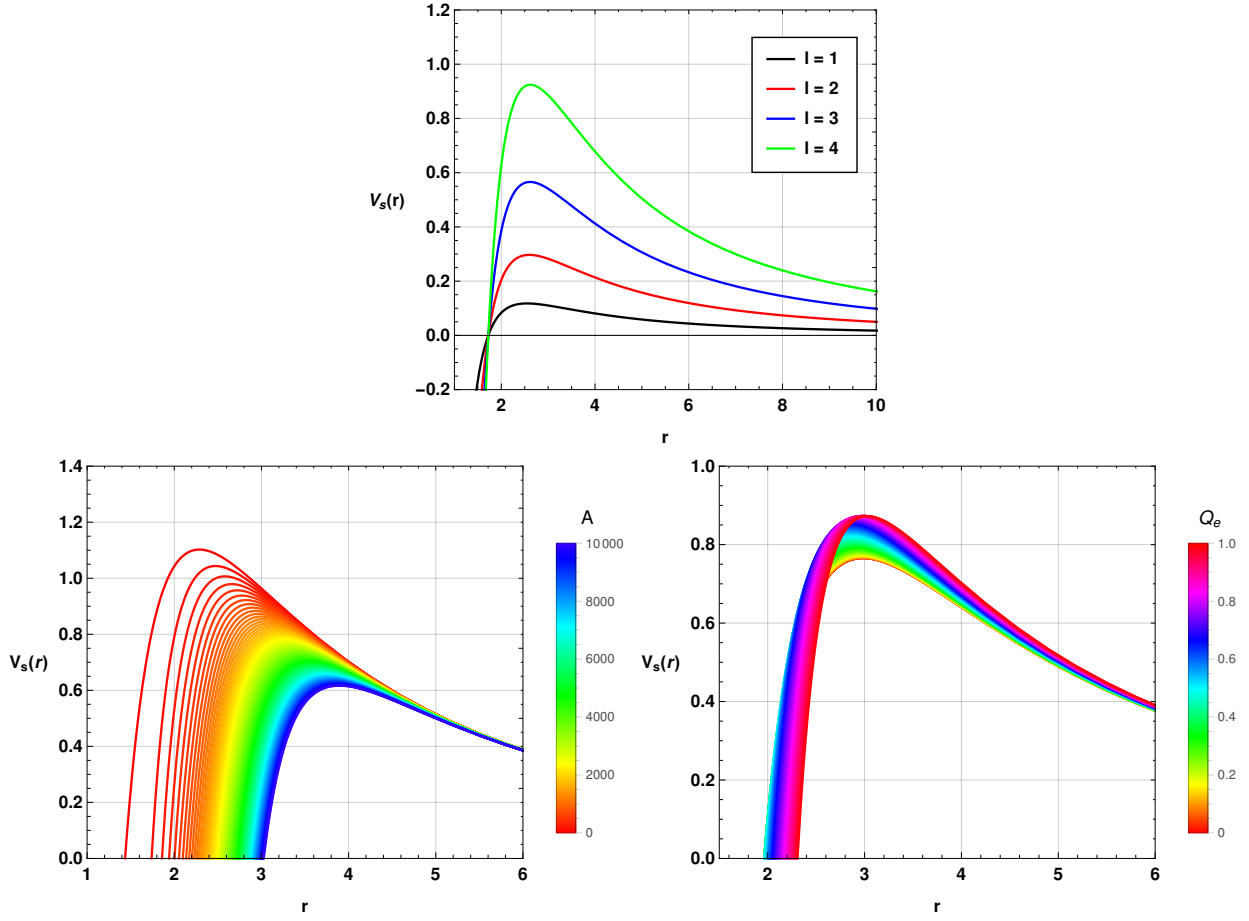


FIG. 10. Variation of scalar potential using $M = 1$ and $a = 0$. On the first panel, $Q_e = 0.7$, $A = 10$, on the second panel, $Q_e = 0.9$, $l = 4$ and on the third panel, $l = 4$ and $A = 1000$ have been used.

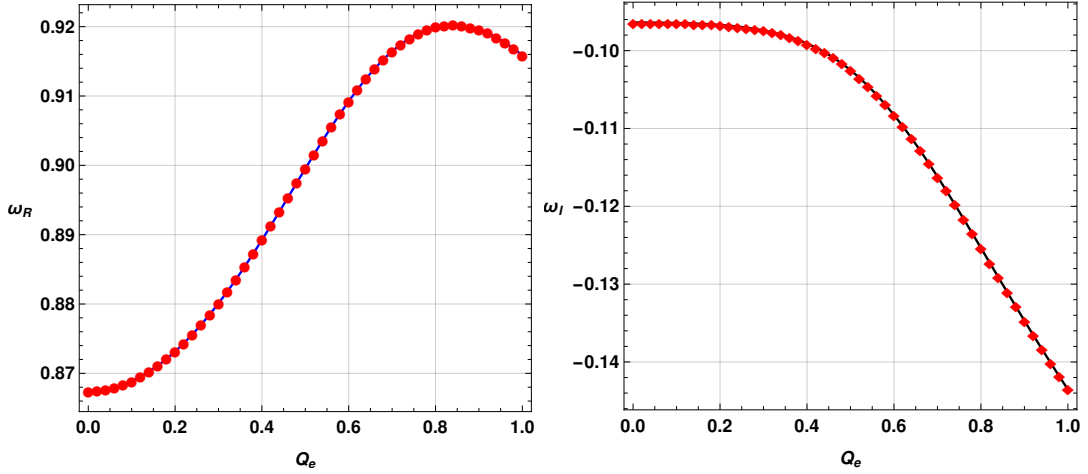


FIG. 11. Variation of real and imaginary QNMs for static black hole using $n = 0$, $M = 1$, $l = 4$ and $A = 1000$.

In this framework, the variable n in Eq. (68) signifies overtone numbers and can take integer values like 0, 1, 2 etc. The value of V_0 is obtained by evaluating the potential function V_s at the location r_{max} , where the potential is at its maximum. At this point, the first derivative of V_s with respect to r is zero, while the second derivative of V_s with respect to r , also evaluated at r_{max} , is denoted as V_0'' [66, 67, 69, 74].

To improve the accuracy of the calculations, additional correction terms, denoted as $\bar{\Lambda}_k$, were included. These terms are

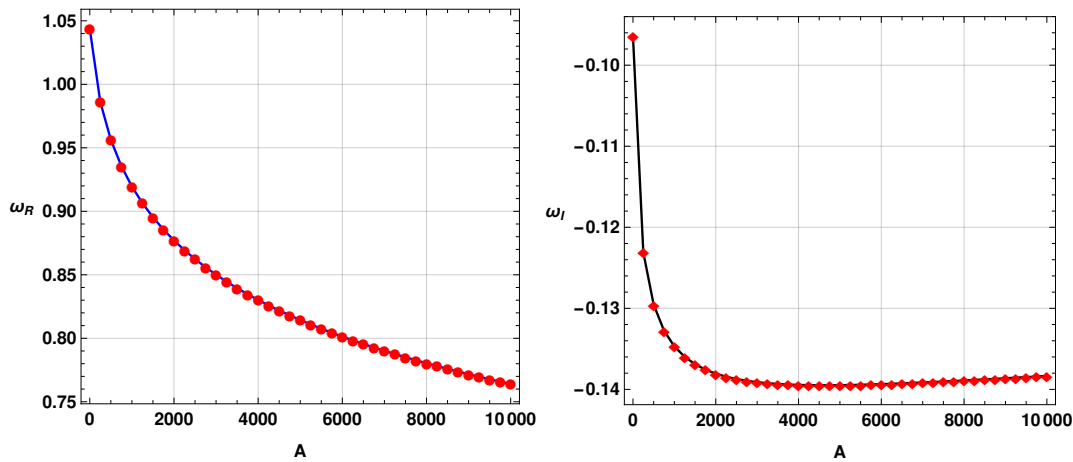


FIG. 12. Variation of real and imaginary QNMs for static black hole using $n = 0$, $M = 1$, $l = 4$ and $Q_e = 0.9$.

explicitly defined in works [64, 69, 74, 75] and account for higher-order effects. These corrections are crucial for accurately predicting the oscillation frequencies of GWs in different astrophysical contexts.

The use of the Padé averaging procedure, combined with these correction terms, significantly enhances the precision of the calculations. The sixth-order WKB method, with these added corrections, is an excellent tool for studying various astrophysical phenomena, including black hole mergers, neutron star oscillations, and cosmic string vibrations. However, due to the complexity of the higher-order numerical WKB method for the case of rotating black holes, we considered only the leading order corrections in the previous subsection. But, as in the case of a static black hole, the situation is comparatively simpler, one can utilise higher-order corrected WKB methods to obtain more precise values of QNMs for the black hole.

We have shown the variation of the QNMs with respect to the model parameter Q_e in Fig. 11. The charge parameter Q_e non-linearly impacts the QNM spectrum. The GW frequency increases non-linearly with an increase in the value of Q_e initially, but from around 0.85, GW frequency starts to decrease. In the case of the imaginary part, we observe that the damping rate of GW increases with an increase in the value of the black hole charge parameter Q_e . One may note that the variation of QNMs is noticeably different from the rotating case.

Finally, in Fig. 12, we have shown the variation of the QNMs with respect to the model parameter A . One can see that the model parameter A has a non-linear effect on the frequencies of ring-down GWs. With an increase in the value of A , the oscillation frequency decreases non-linearly. The damping rate of ring-down GWs increases drastically with an increase in the value of A initially. But beyond the value of A around 5000, we observe a slight decrease in the damping rate with an increase in the value of the model parameter.

VII. CONCLUSION

In this work, we have investigated the properties of black holes when the effects of the screening (described by the parameter A) are taken into account. The latter is interpreted as a dielectric constant in vacuum arising from the one-loop of non-perturbatively quantizing the Euler-Heisenberg nonlinear electrodynamics theory. To this end, we examined its effect on the null regions, such as the horizon and ergosphere, photon-sphere, shadow radius, and observables. Interestingly, the analysis has shown considerable deviation from the Kerr and KN counterparts. The shadow cast reveals that the orbit affected by the screening parameter is the prograde orbit, suggesting that this parameter dominates near the black hole, where the gravitational field is strong.

We also investigated the QNMs for the rotating and static black hole scenarios as another means to probe the photon sphere. We found that for the rotating black hole, the variation of ring-down GWs with respect to the parameter Q_e is almost similar, with a slight variation. However, in the case of damping rate, we observe a non-linear decline with an increase in the parameter Q_e for the rotating black hole, and in the case of the static black hole with $a = 0$, we observe an opposite scenario. The other model parameter A also has noticeable impacts on the QNMs of the black hole. In both rotating and non-rotating scenarios, we observe a decline in the oscillation frequency and an increase in the damping rate with an increase in the values of A . However, the variations in the static case differ slightly. Interestingly, our result still confirms the correspondence between the real part of QNMs and the photon-sphere that is deeply related to the shadow radius R_{sh} (See. Ref. [76]).

VIII. ACKNOWLEDGEMENTS

The work of G.L. is supported by the Italian Istituto Nazionale di Fisica Nucleare (INFN) through the “QGSKY” project and by Ministero dell’Istruzione, Università e Ricerca (MIUR). G.L., A. Ö. and R. P. would like to acknowledge networking support of the COST Action CA18108 - Quantum gravity phenomenology in the multi-messenger approach (QG-MM), COST Action CA21106 - COSMIC WISPerS in the Dark Universe: Theory, astrophysics and experiments (CosmicWISPerS), the COST Action CA22113 - Fundamental challenges in theoretical physics (THEORY-CHALLENGES), and the COST Action CA21136 - Addressing observational tensions in cosmology with systematics and fundamental physics (CosmoVerse).

-
- [1] Kazunori Akiyama *et al.* (Event Horizon Telescope), “First M87 Event Horizon Telescope Results. I. The Shadow of the Supermassive Black Hole,” *Astrophys. J. Lett.* **875**, L1 (2019), [arXiv:1906.11238 \[astro-ph.GA\]](#).
 - [2] Kazunori Akiyama *et al.* (Event Horizon Telescope), “First M87 Event Horizon Telescope Results. IV. Imaging the Central Supermassive Black Hole,” *Astrophys. J. Lett.* **875**, L4 (2019), [arXiv:1906.11241 \[astro-ph.GA\]](#).
 - [3] Kazunori Akiyama *et al.* (Event Horizon Telescope), “First Sagittarius A* Event Horizon Telescope Results. VI. Testing the Black Hole Metric,” *Astrophys. J. Lett.* **930**, L17 (2022), [arXiv:2311.09484 \[astro-ph.HE\]](#).
 - [4] J. L. Synge, “The Escape of Photons from Gravitationally Intense Stars,” *Mon. Not. Roy. Astron. Soc.* **131**, 463–466 (1966).
 - [5] J. P. Luminet, “Image of a spherical black hole with thin accretion disk,” *Astron. Astrophys.* **75**, 228–235 (1979).
 - [6] J. M. Bardeen, “Timelike and null geodesics in the Kerr metric,” in *Les Houches Summer School of Theoretical Physics: Black Holes* (1973) pp. 215–240.
 - [7] Kazunori Akiyama *et al.* (Event Horizon Telescope), “First Sagittarius A* Event Horizon Telescope Results. I. The Shadow of the Supermassive Black Hole in the Center of the Milky Way,” *Astrophys. J. Lett.* **930**, L12 (2022), [arXiv:2311.08680 \[astro-ph.HE\]](#).
 - [8] Kazunori Akiyama *et al.* (Event Horizon Telescope), “First Sagittarius A* Event Horizon Telescope Results. III. Imaging of the Galactic Center Supermassive Black Hole,” *Astrophys. J. Lett.* **930**, L14 (2022), [arXiv:2311.09479 \[astro-ph.HE\]](#).
 - [9] Sunny Vagnozzi *et al.*, “Horizon-scale tests of gravity theories and fundamental physics from the Event Horizon Telescope image of Sagittarius A*,” *Class. Quant. Grav.* **40**, 165007 (2023), [arXiv:2205.07787 \[gr-qc\]](#).
 - [10] Akhil Uniyal, Reggie C. Pantig, and Ali Övgün, “Probing a non-linear electrodynamics black hole with thin accretion disk, shadow, and deflection angle with M87* and Sgr A* from EHT,” *Phys. Dark Univ.* **40**, 101178 (2023), [arXiv:2205.11072 \[gr-qc\]](#).
 - [11] Reggie C. Pantig and Ali Övgün, “Dehnen halo effect on a black hole in an ultra-faint dwarf galaxy,” *JCAP* **08**, 056 (2022), [arXiv:2202.07404 \[astro-ph.GA\]](#).
 - [12] Reggie C. Pantig and Ali Övgün, “Black hole in quantum wave dark matter,” *Fortsch. Phys.* **2022**, 2200164 (2022), [arXiv:2210.00523 \[gr-qc\]](#).
 - [13] Ali Övgün and İzzet Sakallı, “Testing generalized Einstein–Cartan–Kibble–Sciama gravity using weak deflection angle and shadow cast,” *Class. Quant. Grav.* **37**, 225003 (2020), [arXiv:2005.00982 \[gr-qc\]](#).
 - [14] Xiao-Mei Kuang and Ali Övgün, “Strong gravitational lensing and shadow constraint from M87* of slowly rotating Kerr-like black hole,” *Annals Phys.* **447**, 169147 (2022), [arXiv:2205.11003 \[gr-qc\]](#).
 - [15] Ghulam Mustafa, Farruh Atamurotov, Ibrar Hussain, Sanjar Shaymatov, and Ali Övgün, “Shadows and gravitational weak lensing by the Schwarzschild black hole in the string cloud background with quintessential field*,” *Chin. Phys. C* **46**, 125107 (2022), [arXiv:2207.07608 \[gr-qc\]](#).
 - [16] Yashmitha Kumaran and Ali Övgün, “Deflection Angle and Shadow of the Reissner–Nordström Black Hole with Higher-Order Magnetic Correction in Einstein–Nonlinear–Maxwell Fields,” *Symmetry* **14**, 2054 (2022), [arXiv:2210.00468 \[gr-qc\]](#).
 - [17] İrfan Cimdiker, Durmus Demir, and Ali Övgün, “Black hole shadow in symmergent gravity,” *Phys. Dark Univ.* **34**, 100900 (2021), [arXiv:2110.11904 \[gr-qc\]](#).
 - [18] Mert Okyay and Ali Övgün, “Nonlinear electrodynamics effects on the black hole shadow, deflection angle, quasinormal modes and greybody factors,” *JCAP* **01**, 009 (2022), [arXiv:2108.07766 \[gr-qc\]](#).
 - [19] Farruh Atamurotov, Ibrar Hussain, Ghulam Mustafa, and Ali Övgün, “Weak deflection angle and shadow cast by the charged-Kiselev black hole with cloud of strings in plasma*,” *Chin. Phys. C* **47**, 025102 (2023).
 - [20] Sunny Vagnozzi and Luca Visinelli, “Hunting for extra dimensions in the shadow of M87*,” *Phys. Rev. D* **100**, 024020 (2019), [arXiv:1905.12421 \[gr-qc\]](#).
 - [21] Hiroki Yajima and Takashi Tamaki, “Black hole solutions in Euler–Heisenberg theory,” *Phys. Rev. D* **63**, 064007 (2001), [arXiv:gr-qc/0005016](#).
 - [22] Remo Ruffini, Yuan-Bin Wu, and She-Sheng Xue, “Einstein–Euler–Heisenberg Theory and charged black holes,” *Phys. Rev. D* **88**, 085004 (2013), [arXiv:1307.4951 \[hep-th\]](#).
 - [23] Nora Bretón, Claus Lämmerzahl, and Alfredo Macías, “Rotating black holes in the Einstein–Euler–Heisenberg theory,” *Class. Quant. Grav.* **36**, 235022 (2019).
 - [24] Nora Bretón, Claus Lämmerzahl, and Alfredo Macías, “Rotating structure of the Euler–Heisenberg black hole,” *Phys. Rev. D* **105**, 104046 (2022).
 - [25] Daniel Amaro, Claus Lämmerzahl, and Alfredo Macías, “Particle motion in the Einstein–Euler–Heisenberg rotating black hole spacetime,” *Phys. Rev. D* **107**, 084040 (2023).

- [26] Xiao-Xiong Zeng, Ke-Jian He, Guo-Ping Li, En-Wei Liang, and Sen Guo, "QED and accretion flow models effect on optical appearance of Euler–Heisenberg black holes," *Eur. Phys. J. C* **82**, 764 (2022), [arXiv:2209.05938 \[gr-qc\]](#).
- [27] Nora Bretón and L. A. López, "Birefringence and quasinormal modes of the Einstein-Euler-Heisenberg black hole," *Phys. Rev. D* **104**, 024064 (2021), [arXiv:2105.12283 \[gr-qc\]](#).
- [28] Zhi Luo and Jin Li, "Gravitational perturbations of the Einstein-Euler-Heisenberg black hole *," *Chin. Phys. C* **46**, 085107 (2022).
- [29] Heng Dai, Zixu Zhao, and Shuhang Zhang, "Thermodynamic phase transition of Euler-Heisenberg-AdS black hole on free energy landscape," *Nucl. Phys. B* **991**, 116219 (2023), [arXiv:2202.14007 \[gr-qc\]](#).
- [30] Yuanyuan Feng and Weifu Nie, "The Correspondence Between Shadow and the Test Field in a Einstein-Euler-Heisenberg Black Hole," *Int. J. Theor. Phys.* **61**, 223 (2022).
- [31] Marco Maceda and Alfredo Macías, "Non-commutative inspired black holes in Euler–Heisenberg non-linear electrodynamics," *Phys. Lett. B* **788**, 446–452 (2019), [arXiv:1807.05269 \[gr-qc\]](#).
- [32] Marco Maceda, Alfredo Macias, and Daniel Martinez-Carbajal, "Shadow of a noncommutative-inspired Einstein–Euler–Heisenberg black hole," *Int. J. Mod. Phys. A* **36**, 2150191 (2021), [arXiv:2008.07040 \[gr-qc\]](#).
- [33] H. Rehman, G. Abbas, Tao Zhu, and G. Mustafa, "Matter accretion onto the magnetically charged Euler–Heisenberg black hole with scalar hair," *Eur. Phys. J. C* **83**, 856 (2023), [arXiv:2307.16155 \[gr-qc\]](#).
- [34] Farzan Mushtaq, Xia Tiecheng, Allah Ditta, Farruh Atamurotov, Alisher Abduvokhidov, and Alimova Asalkhon, "Weak gravitational lensing and fundamental frequencies of Einstein–Euler–Heisenberg black hole," *New Astron.* **108**, 102185 (2024).
- [35] B. P. Abbott et al. (LIGO Scientific Collaboration and Virgo Collaboration), "Observation of gravitational waves from a binary black hole merger," *Phys. Rev. Lett.* **116**, 061102 (2016).
- [36] C. V. Vishveshwara, "Scattering of Gravitational Radiation by a Schwarzschild Black-hole," *Nature* **227**, 936–938 (1970).
- [37] William H. Press, "Long Wave Trains of Gravitational Waves from a Vibrating Black Hole," *Astrophys. J. Lett.* **170**, L105–L108 (1971).
- [38] Kostas D. Kokkotas and Bernd G. Schmidt, "Quasinormal modes of stars and black holes," *Living Rev. Rel.* **2**, 2 (1999), [arXiv:gr-qc/9909058](#).
- [39] Ángel Rincón and Grigoris Panotopoulos, "Greybody factors and quasinormal modes for a nonminimally coupled scalar field in a cloud of strings in (2+1)-dimensional background," *Eur. Phys. J. C* **78**, 858 (2018), [arXiv:1810.08822 \[gr-qc\]](#).
- [40] Dong Liu, Yi Yang, Ali Övgün, Zheng-Wen Long, and Zhaoyi Xu, "Gravitational ringing and superradiant instabilities of the Kerr-like black holes in a dark matter halo," *Eur. Phys. J. C* **83**, 565 (2023), [arXiv:2204.11563 \[gr-qc\]](#).
- [41] Angel Rincon, P. A. Gonzalez, Grigoris Panotopoulos, Joel Saavedra, and Yerko Vasquez, "Quasinormal modes for a non-minimally coupled scalar field in a five-dimensional Einstein–Power–Maxwell background," *Eur. Phys. J. Plus* **137**, 1278 (2022), [arXiv:2112.04793 \[gr-qc\]](#).
- [42] Ali Ovgün and Kimet Jusufi, "Quasinormal Modes and Greybody Factors of $f(R)$ gravity minimally coupled to a cloud of strings in $2 + 1$ Dimensions," *Annals Phys.* **395**, 138–151 (2018), [arXiv:1801.02555 \[gr-qc\]](#).
- [43] Ali Övgün, İzzet Sakalli, and Halil Mutuk, "Quasinormal modes of dS and AdS black holes: Feedforward neural network method," *Int. J. Geom. Meth. Mod. Phys.* **18**, 2150154 (2021), [arXiv:1904.09509 \[gr-qc\]](#).
- [44] M. A. Anacleto, J. A. V. Campos, F. A. Brito, and E. Passos, "Quasinormal modes and shadow of a Schwarzschild black hole with GUP," *Annals Phys.* **434**, 168662 (2021), [arXiv:2108.04998 \[gr-qc\]](#).
- [45] Gaetano Lambiase, Reggie C. Pantig, Dhruva Jyoti Gogoi, and Ali Övgün, "Investigating the connection between generalized uncertainty principle and asymptotically safe gravity in black hole signatures through shadow and quasinormal modes," *Eur. Phys. J. C* **83**, 679 (2023), [arXiv:2304.00183 \[gr-qc\]](#).
- [46] Yassine Sekhmani and Dhruva Jyoti Gogoi, "Electromagnetic quasinormal modes of dyonic AdS black holes with quasitopological electromagnetism in a Horndeski gravity theory mimicking EGB gravity at $D = 4$," *International Journal of Geometric Methods in Modern Physics*, 2350160 (2023).
- [47] Dhruva Jyoti Gogoi, Ali Övgün, and M. Koussour, "Quasinormal modes of black holes in $f(Q)$ gravity," *Eur. Phys. J. C* **83**, 700 (2023), [arXiv:2303.07424 \[gr-qc\]](#).
- [48] Nashiba Parbin, Dhruva Jyoti Gogoi, Jyatsnasree Bora, and Umananda Dev Goswami, "Deflection angle, quasinormal modes and optical properties of a de Sitter black hole in $f(T, B)$ gravity," *Phys. Dark Univ.* **42**, 101315 (2023), [arXiv:2211.02414 \[gr-qc\]](#).
- [49] Ronit Karmakar, Dhruva Jyoti Gogoi, and Umananda Dev Goswami, "Quasinormal modes and thermodynamic properties of GUP-corrected Schwarzschild black hole surrounded by quintessence," *International Journal of Modern Physics A* **37**, 2250180 (2022).
- [50] Dhruva Jyoti Gogoi and Umananda Dev Goswami, "Quasinormal modes and Hawking radiation sparsity of GUP corrected black holes in bumblebee gravity with topological defects," *JCAP* **06**, 029 (2022), [arXiv:2203.07594 \[gr-qc\]](#).
- [51] Dhruva Jyoti Gogoi, Ronit Karmakar, and Umananda Dev Goswami, "Quasinormal modes of nonlinearly charged black holes surrounded by a cloud of strings in Rastall gravity," *Int. J. Geom. Meth. Mod. Phys.* **20**, 2350007 (2023), [arXiv:2111.00854 \[gr-qc\]](#).
- [52] Dhruva Jyoti Gogoi and Umananda Dev Goswami, "Quasinormal modes of black holes with non-linear-electrodynamic sources in Rastall gravity," *Phys. Dark Univ.* **33**, 100860 (2021), [arXiv:2104.13115 \[gr-qc\]](#).
- [53] Reggie C. Pantig, Leonardo Mastrototaro, Gaetano Lambiase, and Ali Övgün, "Shadow, lensing, quasinormal modes, greybody bounds and neutrino propagation by dyonic ModMax black holes," *Eur. Phys. J. C* **82**, 1155 (2022), [arXiv:2208.06664 \[gr-qc\]](#).
- [54] Dhruva Jyoti Gogoi, "Violation of Hod's conjecture and probing it with optical properties of a 5-D black hole in Einstein Gauss–Bonnet Bumblebee theory of gravity," *Phys. Dark Univ.* **45**, 101535 (2024), [arXiv:2405.02455 \[gr-qc\]](#).
- [55] Dhruva Jyoti Gogoi and Supakchai Ponglertsakul, "Constraints on Quasinormal modes from Black Hole Shadows in regular non-minimal Einstein Yang-Mills Gravity," (2024), [arXiv:2402.06186 \[gr-qc\]](#).

- [56] Dhruva Jyoti Gogoi, Narges Heidari, Jan Kríz, and Hassan Hassanabadi, “Quasinormal Modes and Greybody Factors of de Sitter Black Holes Surrounded by Quintessence in Rastall Gravity,” *Fortsch. Phys.* **72**, 2300245 (2024), [arXiv:2307.09976 \[gr-qc\]](#).
- [57] W. Heisenberg and H. Euler, “Consequences of dirac theory of the positron,” (2006), [arXiv:physics/0605038 \[physics.hist-ph\]](#).
- [58] Daniela Magos, Nora Bretón, and Alfredo Macías, “Orbits in static magnetically and dyonically charged Einstein-Euler-Heisenberg black hole spacetimes,” *Phys. Rev. D* **108**, 064014 (2023).
- [59] Petr Slaný and Zdeněk Stuchlík, “Equatorial circular orbits in Kerr–Newman–de Sitter spacetimes,” *Eur. Phys. J. C* **80**, 587 (2020).
- [60] Brandon Carter, “Global structure of the Kerr family of gravitational fields,” *Phys. Rev.* **174**, 1559–1571 (1968).
- [61] Tim Johannsen, “Photon Rings around Kerr and Kerr-like Black Holes,” *Astrophys. J.* **777**, 170 (2013), [arXiv:1501.02814 \[astro-ph.HE\]](#).
- [62] Kenta Hioki and Kei-ichi Maeda, “Measurement of the Kerr Spin Parameter by Observation of a Compact Object’s Shadow,” *Phys. Rev. D* **80**, 024042 (2009), [arXiv:0904.3575 \[astro-ph.HE\]](#).
- [63] Irina Dymnikova and Kirill Kraav, “Identification of a Regular Black Hole by Its Shadow,” *Universe* **5**, 163 (2019).
- [64] Sai Iyer and Clifford M. Will, “Black Hole Normal Modes: A WKB Approach. I. Foundations and Application of a Higher Order WKB Analysis of Potential Barrier Scattering,” *Phys. Rev. D* **35**, 3621 (1987).
- [65] Oscar J. C. Dias, Mahdi Godazgar, and Jorge E. Santos, “Eigenvalue repulsions and quasinormal mode spectra of Kerr-Newman: an extended study,” *JHEP* **07**, 076 (2022), [arXiv:2205.13072 \[gr-qc\]](#).
- [66] R. A. Konoplya, A. Zhidenko, and A. F. Zinhailo, “Higher order WKB formula for quasinormal modes and grey-body factors: recipes for quick and accurate calculations,” *Class. Quant. Grav.* **36**, 155002 (2019), [arXiv:1904.10333 \[gr-qc\]](#).
- [67] R. A. Konoplya and A. Zhidenko, “Quasinormal modes of black holes: From astrophysics to string theory,” *Rev. Mod. Phys.* **83**, 793–836 (2011), [arXiv:1102.4014 \[gr-qc\]](#).
- [68] R. A. Konoplya and Z. Stuchlík, “Are eikonal quasinormal modes linked to the unstable circular null geodesics?” *Phys. Lett. B* **771**, 597–602 (2017), [arXiv:1705.05928 \[gr-qc\]](#).
- [69] R. A. Konoplya, “Quasinormal behavior of the d-dimensional Schwarzschild black hole and higher order WKB approach,” *Phys. Rev. D* **68**, 024018 (2003), [arXiv:gr-qc/0303052](#).
- [70] Huan Yang, David A. Nichols, Fan Zhang, Aaron Zimmerman, Zhongyang Zhang, and Yanbei Chen, “Quasinormal-mode spectrum of Kerr black holes and its geometric interpretation,” *Phys. Rev. D* **86**, 104006 (2012), [arXiv:1207.4253 \[gr-qc\]](#).
- [71] S. A. Teukolsky, “Rotating black holes - separable wave equations for gravitational and electromagnetic perturbations,” *Phys. Rev. Lett.* **29**, 1114–1118 (1972).
- [72] Raimon Luna, Juan Calderón Bustillo, Juan José Seoane Martínez, Alejandro Torres-Forné, and José A. Font, “Solving the Teukolsky equation with physics-informed neural networks,” *Phys. Rev. D* **107**, 064025 (2023), [arXiv:2212.06103 \[gr-qc\]](#).
- [73] Huan Yang, “Relating Black Hole Shadow to Quasinormal Modes for Rotating Black Holes,” *Phys. Rev. D* **103**, 084010 (2021), [arXiv:2101.11129 \[gr-qc\]](#).
- [74] Jerzy Matyjasek and Malgorzata Telecka, “Quasinormal modes of black holes. II. Padé summation of the higher-order WKB terms,” *Phys. Rev. D* **100**, 124006 (2019), [arXiv:1908.09389 \[gr-qc\]](#).
- [75] Bernard F. Schutz and Clifford M. Will, “BLACK HOLE NORMAL MODES: A SEMIANALYTIC APPROACH,” *Astrophys. J. Lett.* **291**, L33–L36 (1985).
- [76] Vitor Cardoso, Alex S. Miranda, Emanuele Berti, Helvi Witek, and Vilson T. Zanchin, “Geodesic stability, Lyapunov exponents and quasinormal modes,” *Phys. Rev. D* **79**, 064016 (2009), [arXiv:0812.1806 \[hep-th\]](#).